Available online at www.sciencedirect.com
ScienceDirect
International Journal of Heat and Fluid Flow 28 (2007) 616–629
International Journal of HEAT AND FLUID FLOW
www.elsevier.com/locate/ijhff

Description of flow field in the wheelhouses of cars

Tamas Regert *, Tamas Lajos

Budapest University of Technology and Economics, Faculty of Mechanical Engineering, Department of Fluid Mechanics, H-1111 Budapest Bertalan L. u. 4-6, Hungary

Received 18 October 2006; received in revised form 24 April 2007; accepted 25 April 2007
Available online 6 June 2007

Abstract

RANS and URANS modeling of flow past simplified vehicle bodies with wheelhouses and rotating wheels have been carried out in order to understand the flow phenomena through detailed analyses of flow in the wheelhouses. The vortex skeleton method was used to characterize the flow structure. The second invariant of the velocity gradient tensor (Q) and iso-surfaces of total pressure have been applied for detecting dynamically significant vortical structures. It was found that the flow field in the wheelhouse can be characterized by several large recirculation zones, of which six can be classified as qualitatively independent of the grid, numerical scheme, turbulence model and the shape of the vehicle body. The change of flow field structure was investigated for various wheelhouse geometries, and for closed lower and/or lateral gaps between the wheelhouse and the external flow field. Aerodynamic forces acting on the body, wheelhouse and wheel were determined separately for different configurations.

Keywords: Aerodynamics; Car; Wheelhouse; Wheel; CFD; Flow-topology

1. Introduction

Road vehicle aerodynamics seems to reach its limits in terms of body shape optimization. Basic low-drag body shapes were developed during the last few decades (Hucho, 1998). The effect of rotating wheels exposed to a free stream, or being partially covered by the car wheelhouse, leads to a dramatic increase in drag coefficient through mechanisms that are still not fully understood. Also wheels influence mud deposition on the vehicle body (Lajos et al., 1984) and are important elements of the underbody flows (Wiedemann, 1996; Lajos et al., 1988). The contribution of the wheels and wheelhouses to the total aerodynamic drag and lift of a modern car is around 30% and 40%, respectively (Wickern and Zwicker, 1995; Eloffson et al., 2002; Merker and Berneburg, 1992). Road vehicles, especially their wheels and wheelhouses are bluff bodies, characterized by large regions of flow field influenced by boundary layer separation. The resultant flow field is a complex, 3D flow field. The Reynolds number is in the order of 8×10^5, thus transition occurs far upstream from the wheelhouses so the flow is handled to be turbulent. The fluid can be regarded as incompressible and isothermal.

Experiments have already been carried out in the past decades to investigate full-scale cars (Wickern and Zwicker, 1995), scale-model passenger cars (Eloffson et al., 2002; Merker and Berneburg, 1992), and idealized car models (Fabijanic, 1996; Skea et al., 2000; Cogotti, 1983). On the basis of experimental results, some assumptions have been made about the flow mechanisms, but a detailed structure of the flow field in this region has still not been published. Eloffson et al. (2002) made an experimental parameter study on a scale-model Volvo passenger car, changing the geometry of the rear spoiler and the mud flap behind the rear wheel. They observed significant changes in drag that indicated the importance of the interaction between the wake of the wheel and flow in the wheelhouse, as well as the wake of the body. The first parameter study of wheels in wheelhouses was made by Cogotti (1983), who used a

* Corresponding author.
E-mail addresses: regert@ara.bme.hu (T. Regert), lajos@ara.bme.hu (T. Lajos).

0142-727X/$ - see front matter © 2007 Elsevier Inc. All rights reserved.
doi:10.1016/j.ijheatfluidflow.2007.04.017

simplified streamlined body with only one pair of wheels (one axis and two wheels) with wheelhouses in a fixed ground wind tunnel (a small ground clearance allowed wheel rotation). The geometry of the wheelhouses was variable. Another parameter study was carried out by Fabijanic (1996) on the effect of wheelhouse geometry on the forces acting on the vehicle, using a simplified body that had also only one pair of wheels with one axis. Fabijanic's model was not as streamlined as Cogotti's one, it was characterized by a base of forced boundary layer separation. Due to the complexity of the flow, only a few measured quantities are available for comparison with the CFD results. Such parameters are the integral parameters (lift and drag coefficients) and the surface pressure distributions. These parameters are obviously not enough to give a full insight into the flow characteristics and the mechanisms governing them but details regarding the velocity field inside wheelhouses have not been published, to the knowledge of the authors. To some extent, the authors aimed to apply validation based synergy of CFD and experimental results, where CFD has the advantage of visualizing the inner flow domain. This kind of approach for investigating complex flow phenomena was also discussed by Hanjalić (2005).

2. Description of flow modeling

2.1. On the applicability of RANS and URANS concept

For modeling the flow field in wheelhouses of cars, the commercial code Fluent 6 was used, with which steady and unsteady state computations were carried out applying RANS and URANS approach, respectively. Turbulent flow around bluff bodies is known to be in principle unsteady and thus, for sufficiently fine grid resolution, the governing equations of the flow have no steady solution. For grid resolutions coarser than the required level for resolving small scale unsteadiness, steady solution can be obtained if there is no characteristic large scale vortex shedding phenomenon. However, large scale unsteadiness can be traced by means of URANS simulations. In the corresponding literature there are few cases of unsteady simulation of the flow field around isolated road wheels (Basara et al., 2000; McManus and Zhang, 2006; Hedges et al., 2002). However, mainly due to the fact that the large scale vortical elements of the flow field around an isolated road wheel are quasi-steady, longitudinal (open) vortical structures, good agreement was found between experiments and steady RANS modeling results in the work of Skea et al. (1998), Skea et al. (2000) and Axon et al. (1999). Recognizing the well-known deficiencies of linear eddy-viscosity turbulence models at describing the Reynolds stresses, and at determining location of boundary layer separation and reattachment length for known test cases due to the application of not always correct wall-treatments, this investigation aims to provide strictly a qualitative model of the flow field without making statements on the size and exact location of recirculation zones. The effect of the anisotropy of Reynolds stresses inside the flow domain, away from walls was, however, considered by using a Reynolds stress model for the computations as well as the linear eddy viscosity models.

2.2. Details of the URANS computations

URANS simulations were carried out using two turbulence models but for the same near-wall handling (non-equilibrium wall functions) concept on a vehicle based on the model used by Fabijanic (1996) (Fig. 3b). The unstructured mesh consisted of 4 million cells including prismatic layers on the wall surfaces with the first cell size tuned to $y^+ = 30$ and with an expansion ratio of 1.2. The number of the prismatic layers was determined by matching the volumes of the elements of the last prism layer to the neighboring tetrahedral cell elements to avoid a jump in cell sizes. This resulted in 1.5 million cells inside the wheelhouse only. Although boundary layer separation depends mainly on the near-wall-handling approach, vortex shedding is expected to form in the inner domain well away from walls where the rotating masses of fluid might include anisotropic regions, thus beside the linear 'realizable' k–ε model, the full Reynolds stress model (RSM) was also applied for the URANS approach. For the unsteady runs CFL $\sim$0.5 was applied for the 'realizable' k–ε model while CFL $\sim$ 0.4 was used for the more unstable RSM and discretization in time was second order accurate. The runs were initialized from a steady solution.

As the timescale of the vortical structures is very different in the free stream and in the wheelhouse, the total computed time period was 20 wheel diameters flow-through with the velocity inside the wheelhouse which was approximately 20% of the free stream velocity and 70 wheel diameters computed with the free stream velocity, to ensure the onset of large scale unsteadiness if it should exist. Concerning the time history of the drag coefficient, after a slight initial modulation (with an amplitude of approximately 2% of the mean value), in which time the flow passes some 30 wheel diameters, the drag coefficient levels off with time. A slight pulsation of the longitudinal vortex structures can be observed during the aforementioned modulation but after leveling off, the topology of the flow field is qualitatively unchanged and is virtually insensitive to the two applied turbulence models. However, in case of the 'realizable' k–ε model, even the modulation is missing and the drag coefficient keeps its steady value and the pulsation of the vortical structures is also substantially weaker, even hardly visible.

2.3. Turbulence modeling

For the RANS modeling, the 'realizable' k–ε model (Shih et al., 1995), the SST k–ω (Menter, 1994), and Reynolds stress modelschemes were applied. All three are claimed to have the ability of predicting characteristics of

separated flows, to some extent. A comparison between the results obtained by using 'realizable' k–ε and SST k–ω turbulence models with full resolution of the boundary layer ($y^+ = 1$) can be seen in Fig. 1 which shows the pressure coefficient distribution along the centerline of a rotating isolated wheel in contact with the moving ground. It is well known that for full resolution of the computational domain at the wall, where the ω equation begins to play a dominant role, the k–ω model gives more realistic results than the 'realizable' k–ε model which is replaced by the less sophisticated one-equation model of Wolfshtein (1969) in Fluent's solver. If the flow can be characterized by a certain amount of unsteadiness then the k–ω model, which is more correct in the vicinity of wall surfaces, is more likely to capture it, although incorrectly in the case of steady state simulations; indeed the observation of McManus and Zhang (2006) is noted that there is no converged steady solution of the governing equations and residuals show a chaotically oscillating nature. This can be traced on the "instantaneous" pressure coefficient distribution computed by using the SST k–ω model as it has two depression peaks at the top of the wheel between 250° and 300°. In the case of the 'realizable' k–ε model there is only one depression peak and the leveling off of residuals during iteration indicates that, with the 'realizable' k–ε model, one obtains steady solution. However, equally obviously, the agreement is quite good for almost all parts of the wheel periphery except for the aforementioned top region between 250° and 300°.

Nevertheless, the experiments, which range over almost 30 years, differ from each other in this region (250–300°), although Mears et al. (2002) tried to reproduce the experimental conditions of Fackrell and Harvey (1973) exactly. The ambiguous results are blamed on unsteadiness on the top of the wheel and where mean flow properties are so very sensitive to the averaging techniques applied, and further complicated by the rotation period of the wheel and so the co-rotating pressure taps.

For the validation and in the parameter studies for the case of the wheel rotating inside a wheelhouse, described below the 'realizable' k–ε model was used since that turbulence model proved to be acceptably accurate in calculating the aerodynamic forces (Rodi, 1997); however less agreement with the structure of flow field can be achieved by it. The results of the SST k–ω model shows a better flow-field pattern but, for both turbulence models, only the dominant vortical structures are reliable, fine details of the flow field vanish when using any of the existing turbulence models, regardless of their linear or non-linear nature (Leschziner, 2006; Schmidt and Thiele, 2002; Liu et al., 2006). The same cases were computed using the full Reynolds stress model, as well. No significant change in the qualitative structure of the flow field was observed for any of the models. This result might be also a consequence of the near-wall model, as the non-equilibrium logarithmic wall function approach was used near the walls for all wheel-in-wheelhouse cases.

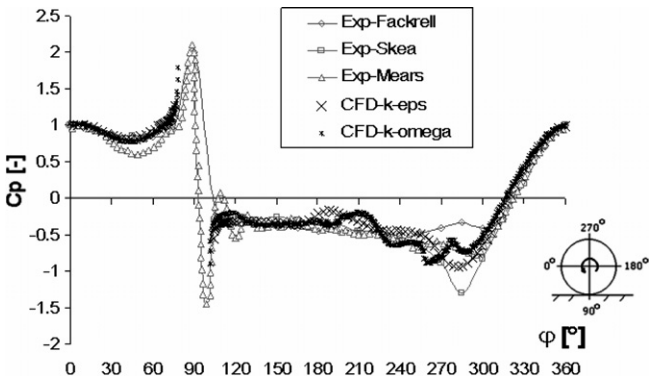

Fig. 1. Pressure coefficient distribution over the periphery of an isolated rotating wheel (aspect ratio = 0.5) (Régert and Lajos, 2003).

2.4. Near-wall handling concept and its effect on the results

It is well known that flow field elements that originate from boundary layer separation from smooth curved surfaces depend significantly on the near-wall treatment. As has been shown in most published works on modeling separated flows, the usual problems arise in applying wall functions and/or low-Reynolds number turbulence models as boundary conditions and near-wall substitution of linear eddy viscosity models, respectively, if the purpose is the prediction of location of boundary layer separation from smooth curved surfaces and/or separation bubble lengths. Due to the high Reynolds number applying for road vehicles, in the present computations the wall function approach was used. The non-equilibrium wall-function approach was shown to give a good approximation of the pressure distribution on the surfaces of isolated road wheels in the work of Skea et al. (1998). The present authors also applied both non-equilibrium wall functions (with $y^+ \sim 30$) and low-Reynolds number turbulence modeling (with $y^+ \sim 1$, based on the model of Wolfshtein, 1969) for the case of rotating isolated road wheels and found discrepancies at the top of the wheel (obviously in the region of boundary layer separation) where both approaches predicted the location of separation further downstream than the point determined from the experiments of Fackrell and Harvey (1973); but there was only a 5–10° difference between the two approaches. Due to this difference the depression peak in the case of non-equilibrium wall functions is 12% higher in absolute value than that in case of fully resolved boundary layer influencing primarily the lift force. However, in all other parts of the wheel's centerline, especially in the more critical wake region, the agreement of pressure distributions was reasonably good (see Fig. 1), i.e. the value of the almost uniform distribution of base pressure was practically the same. This indicates that the base pressure is weakly sensitive to the boundary layer separation occurring on the top of the wheel but mostly influenced by the large longitudinal pair of vortices

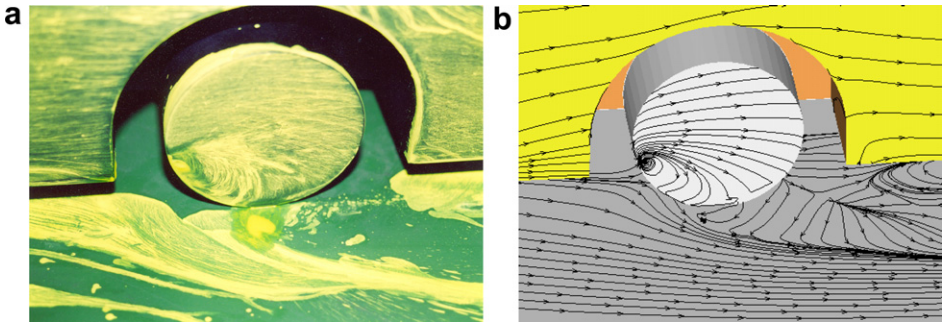

Fig. 2. Flow at a stationary wheel and ground: (a) oil-film visualization in wind tunnel; (b) numerical simulation (wall streak lines).

originating from the separation of boundary layer from the sides of the wheel along its downstream upper side-edges.

2.5. Boundary conditions and computational domain

The size of computational domain was set with regard to its effect on the results; thus, the inlet surface was placed $5L$ in front of, and the outlet surface $10L$ behind the vehicle model (where L is the length of the body). The top and side of the computational domain was placed $5L$ away from the body. Boundary conditions were: uniform velocity distribution at the inlet surface, uniform static pressure at the outlet face, no-slip boundary condition on the walls, slip-wall (symmetry) boundary conditions for the side and top surfaces of the domain. For the computations only half of the geometry was modeled, thus, in the case of URANS modeling, only the processes in the vicinity of the wheelhouse are regarded as being modeled properly.

2.6. Discretization and numerical grid

The convective and diffusion terms in the governing equations were discretized by the second-order upwind scheme. Gradients were computed based on the cell nodes. For pressure–velocity coupling the SIMPLE method was used for the linear eddy-viscosity models while the time marching based pressure–velocity coupling of Fluent 6 was applied for the Reynolds stress model runs. Computation was carried out until residual and drag coefficient curves leveled off with the iteration progress. The numerical grid was unstructured and consisted of tetrahedral elements with prism layers attached to the wall surfaces for the models represented in Fig. 3a and b, while a hexahedral mesh was used in the case of Fig. 3c and d. The resolutions of the computational domains expressed in number of cells were: 500,000 cells for Fig. 3a, 1.2 million and 4 million cells for Fig. 3b (grid dependency check), while 650,000 and 825,000 cells were employed for Fig. 3c (grid dependency check) and 900,000 cells for Fig. 3d.

2.7. Validation of integral quantities

Besides the pressure distribution in the central plane of the wheel reported in Fig. 1, integral quantities (lift and drag coefficients) which were measured by Fackrell and Harvey (1973), Skea et al. (1998) and Mears et al. (2002), (where the last aimed to reproduce Fackrell's experiment), were compared with computational results.

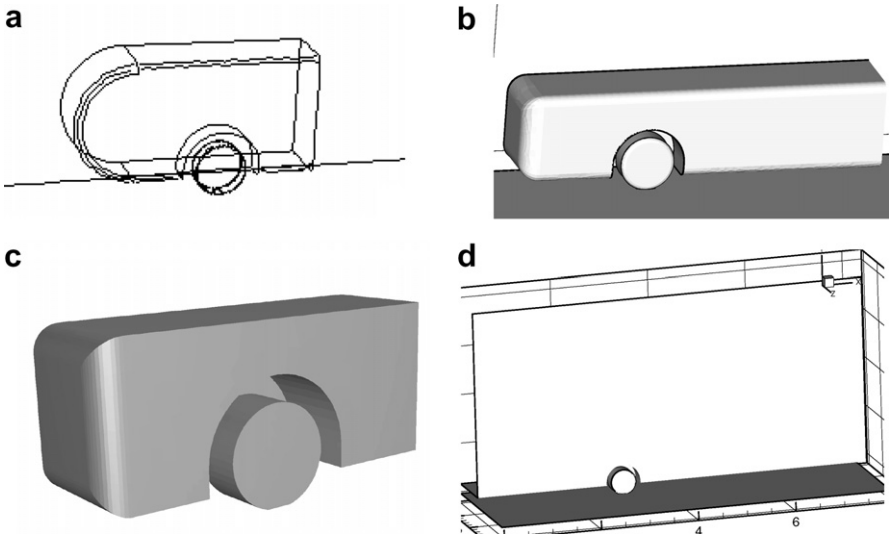

Fig. 3. Body geometries for investigation of flow in wheelhouses.

The pressure distribution on the whole surface of the wheel is validated via its integral leading to drag and lift coefficients. For the stationary wheel, the measured drag and lift coefficients were in the range $C_D = 0.76 \pm 15\%$ and $C_L = 0.77 \pm 15\%$ (Fackrell and Harvey, 1973; Skea et al., 1998; Mears et al., 2002; Axon et al., 1998), respectively, where the extent of the range of coefficients indicates the difference between the measurement results of the previously mentioned publications. For the rotating wheel, the same properties were typically $C_D = 0.58 \pm 15\%$ and $C_L = 0.44 \pm 15\%$ (Fackrell and Harvey, 1973; Skea et al., 1998; Mears et al., 2002; Axon et al., 1998). For the stationary wheel, numerical simulation resulted in a prediction of lift and drag coefficient within 10–15% and ±10% range around the measured mean values, respectively. In the case of the rotating wheel, the drag and lift coefficients were estimated within 8–10% and 15–20% of the mean of the measured drag and lift values, respectively.

Flow past the wheel in a wheelhouse was simulated also for validation purposes. For quantitative validation the experiment of Fabijanic (1996) was taken as a basis. The vehicle model of Fabijanic (1996) is shown in Fig. 3b. Fabijanic (1996) used a moving belt to simulate the moving ground, and the aerodynamic forces acting on the body and the wheels were measured separately. The Reynolds number based on the diameter of the wheel and the free stream velocity was 1.52×10^5. Since no information was published about the structure of the flow field, the validation was made with comparison of integral quantities like aerodynamic drag and lift.

The CFD modeling of the flow past the Fabijanic (1996) model gave relatively good agreement with the experiments (see Table 1).

In Table 1, the lift and drag coefficients of the wheel were related to the streamwise projection of the front surface of the whole vehicle and to the head of free stream velocity. In Table 1, CFD computations under-predicted both values. The discrepancy in lift coefficients is – according to the discussion with the author of Fabijanic (1996) – presumably not due to wrong computations, but due to lack of accurate data about the experimental arrangement. It is also worthwhile mentioning that the absolute value of the lift coefficient is extremely low, thus very small differences lead to very high discrepancies when expressed in terms of percentage. Regarding velocity profiles, to the authors' knowledge, there are no existing detailed flow field data for the case of a wheel in a wheelhouse available in the open literature, thus validation at a deeper level is not yet possible.

In order to verify the numerical modeling used, grid dependence was checked by halving the size of cells inside the wheelhouse; however, the method of wall treatment was not changed. The details of the flow field which are of principal interest in the present investigation are not sensitive to grid resolution above a reasonable level (ranging from 500,000 cells to 1.5 million cells). The value of the drag coefficients for the two grids agreed with each other within 0.5%.

Table 1
Experimental and CFD values for drag and lift coefficient of the wheel of Fabijanic's vehicle model

	C_{Lw}	C_{Dw}
Experiment	0.02 ± 0.007	0.038 ± 0.008
CFD (authors')	0.007 ± 0.001	0.034 ± 0.001
Difference ΔC (%)	$\sim -0.013(-65\%)$	$\sim -0.042(-11\%)$

Parameter studies were carried out by changing the main parameters influencing the flow: the depth (B) and diameter (D) of the wheelhouse related to the width (b) and diameter (d) of the wheel, respectively (see Fig. 4). In parameter studies the simplified car model shown in Fig. 3a was used. The basic topological features of the bodies used for the CFD investigations were similar to those used in the experiments: there was only one pair of wheels and the surface of the underbody was smooth.

The simulation results were compared to the experimental results of Fabijanic (1996) (also in good agreement with Cogotti, 1983). The geometries of the vehicle bodies, the change of aerodynamic force coefficients of which are shown in Fig. 5, are different from each other (see Fig. 3a and b) but the flow characteristics are similar: e.g. an attached flow on the surface of the vehicle upstream of the wheel. Here, in Fig. 5, changes in the drag and lift coefficients are plotted against the relative diameter (D/d) and width (B/b) of the wheelhouses. ΔC values indicate differences of the coefficients belonging to vehicle-model configurations with wheel and wheelhouse to those belonging to configurations with no wheel and no wheelhouse. The agreement is good in both the tendency and the quantitative values. A linear trend-line was fitted to the CFD data. Deviation of the CFD values from this line is very close to that of the experimental values.

2.8. Validation of qualitative characteristics

Flow past a simplified vehicle model with wheelhouse and stationary wheel and ground was investigated by the first author (Régert, 2003) in a wind tunnel with flow visualization by using the oil-film method. Flow past the same arrangement (geometry, Reynolds number, boundary conditions) was also calculated. The results of flow visualization and simulation are compared in Fig. 2. The qualitative agreement of the observed oil-film pattern and wall shear stress lines (streak lines) is quite good, reinforcing the reliability of the CFD simulation used.

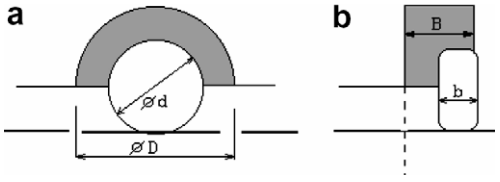

Fig. 4. Tested parameters of wheelhouse geometry.

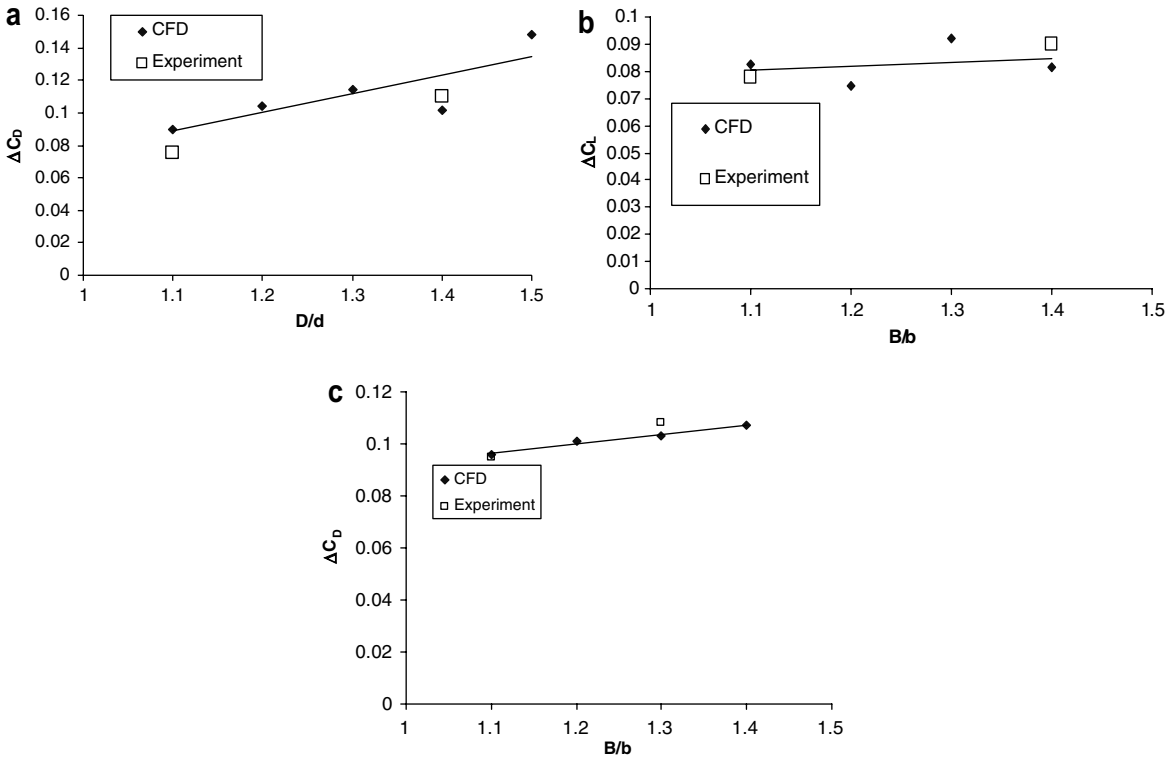

Fig. 5. Comparison of numerical parameter studies with experimental ones (Fabijanic, 1996).

The authors aimed to determine the large scale structures predominantly influencing the flow (while acknowledging that secondary separations that can be characterized by much less kinetic energy would be expected to vanish due to the incorrect behavior of these turbulence models in adverse-pressure-gradient flows). From comparing the results of numerical simulations and experiments as well as regarding the results of various verifications of the models used – in accordance with the general practice reported in the literature – it may be concluded that the numerical modeling of the flow used describes the real flow processes to an acceptable accuracy and reliability for qualitative analysis.

2.9. Vehicle models used for the investigation of the flow field

In the frame of this investigation four different simplified body geometries were studied. The geometries investigated are shown in Fig. 3. The diameter of the wheels for the cases shown in Fig. 3a, c and d was 0.5 m, while for b it was 0.076 m according to the experiments of Fabijanic (1996). All investigations were made in a reference frame fixed to the vehicle body. The Reynolds number based on the free stream velocity and the diameter of the wheel varied in the range of 1.52×10^5–8.5×10^5.

Fig. 3a shows a fore-body different from that of the other two cases. This body geometry was chosen to determine the effect of the shape of the fore-body on flow in the wheelhouse. The models shown in Fig. 3b and c have a similar fore-body shape but the distance between the wheel and the front of the vehicle is smaller in the case of Fig. 3c than in the case of Fig. 3b (Fabijanic, 1996 model). In the case of the model in Fig. 3d the body in front of the wheel is infinite long.

3. Characteristics of flow field in the wheelhouse

3.1. A model for description of the flow in vehicle wheelhouses

A 3D, complex flow field develops in the wheelhouse. To understand this flow field and to identify the effect of, for example, geometrical changes on it, a qualitative structure model has been used for its description. In doing this the first task is to identify the elements of the flow that are substantial in the development of the flow field. In flows dominated by boundary layer separation vortices essentially determine the flow field, so the vortex skeleton (Perry and Hornung, 1984) method was used, where the flow field is described by position, size and shape of vortices.

The vortex skeleton model of the wheelhouse flow field consisting of vortex filaments (tubes) identified by capital letters is shown in Fig. 6. The direction of flow in these vortices and recirculation zones is indicated by lines with arrows. The cross-section of the filaments characterizes the size of the core region of vortices and their change.

The vortex filaments were defined by using several methods simultaneously. The traditional representation of the flow field: plotting of streamlines (or path lines) gives valuable information about the position, size of recirculation

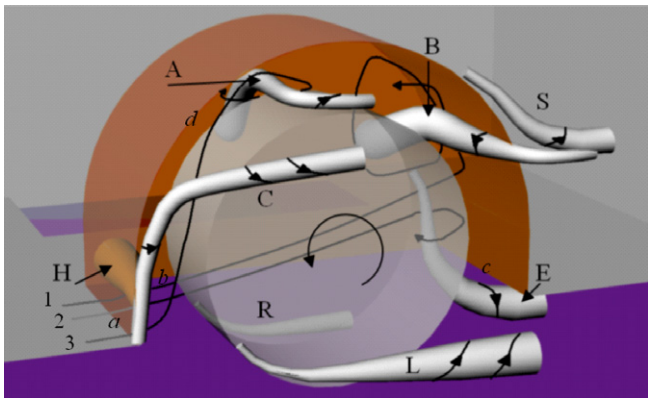

Fig. 6. Vortex skeleton model of the wheelhouse flow field.

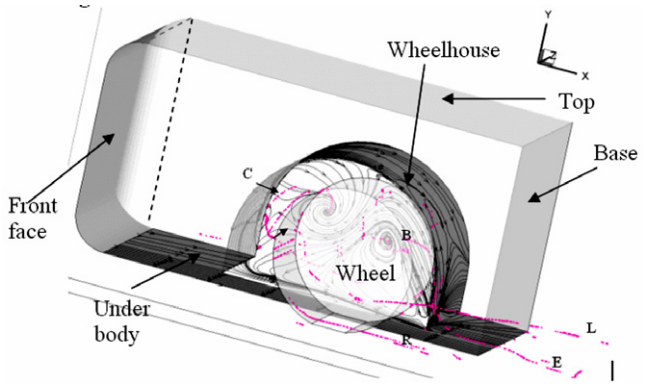

Fig. 7. Vortex filaments in a wheelhouse, underbody flow determined by using the critical point method. Wall streak lines are visible on the surfaces of the model. Flow from left to right, view from outside.

zones, the velocity direction and the origin of fluid particles flowing through the flow structure under consideration. The strength of the vortices determining their influence on the overall flow field was determined by analysis of other quantities. Vortices can be detected by analysis of the distribution of Q (Jeong and Hussain, 1995), the second invariant of the velocity gradient tensor expressing the domination of "swirling" flow as opposed to deformation. A further characteristic of vortices is the low total pressure (head) inside them, so tube-shaped iso-total pressure surfaces of small values indicate the presence of vortices. The method of critical points (Perry et al., 1990) was also used to identify vortices.

The iso-surfaces of Q and total pressure (head) will be shown and discussed in Figs. 9–11 of Section 3.7. Fig. 7 shows vortex filaments determined by the critical point method.

The analysis of wall streak-lines can also help in detecting vortices (Fig. 7). The base points of vortices, separation and reattachment lines of boundary layer can be recognized in Fig. 7.

The vortex filaments and tubes shown in Fig. 6 were determined by simultaneous application of the methods listed above. By analyzing three different simplified vehicle bodies, eight larger flow structures (vortices) were detected in the wheelhouses the position as well as the size and strength of which depends on the wheelhouse geometry.

In the following sections the way of formation, characteristics, effect on the flow field of individual flow field structures shown in Fig. 6 will be discussed. The whole flow field will be divided into four interconnected parts.

3.2. Flow in the underbody gap

It is a well-known phenomenon (Wiedemann, 1996; Fabijanic, 1996; Hucho, 1998) that the distance between the front face and the wheel considerably influences the yaw angle of the wheel-approaching flow in the vicinity of the underbody: the closer the wheelhouse is situated to the front face of the vehicle, the bigger is the yaw angle. It will be shown below that the characteristics of the flow field are substantially controlled by this yaw angle.

The yaw angles of the wheel approaching flow for models of different fore-body lengths were:

- 1D fore-body length (Fig. 3c) $\alpha = 9.18°$.
- 2D fore-body length (Fig. 3b) $\alpha = 7.5°$.
- infinite fore-body length (Fig. 3d) $\alpha = 2.85°$.

The lower part of the wheel, not covered by the wheelhouse, is exposed to the flow in the underbody gap. When comparing the flow past the lower part of the wheel in the wheelhouse with that of an isolated wheel, it was concluded that they resemble each other very closely. This observation is in accordance with the experiences of Morelli (1969). Outside the wheelhouse, near the ground, attached to the lower part of the wheel, two permanently existing longitudinal (open) vortices can be observed – similar to the case of an isolated wheel – marked with L and R (see Fig. 6). The reason for the development of these vortices is separation of the boundary layer of the lateral outflow from the narrowing gap between the rolling wheel and the ground over the edges of the wheel-running surface, close to the ground where the angle between these edges and the direction of flow velocity in the underbody gap is small. The separation bubbles attached to these edges are stretched by the underbody flow, so the separation bubbles become vortices extending into the underbody gap and wake of the vehicle model. (Similar flow structures (vortices) originate from open separation bubbles attached to the slanted C-pillar of fastback cars.) The existence of these vortices is practically independent of the vehicle geometry, and their size and position depends on the profile of the wheel and the yaw angle of the wheel-approaching flow.

3.3. Upstream part of the wheelhouse

Air enters the wheelhouse below and around three sections of the leading edge, "a" in Fig. 6, and, because of the slanted wheel approaching flow, also below and around

the longitudinal edge, "b". Air entering the wheelhouse below Section 1 (close to the inner wall of the wheelhouse) flows slightly upwards and will be deflected upwards by the downstream part of the wheel arch in case when there is no wheel axis, then gives rise to vortex (recirculation zone) B (see Fig. 6). The base point of this vortex is shown to the right of Fig. 7. The sense of rotation of vortex B corresponds to that of the wheel. The existence of this vortex (B) is declared to be uncertain due to its sensitivity to the mechanical details of the wheel suspension.

Air entering the wheelhouse below Section 2 of edge "a" flows close to the inner side of the wheel and will be deflected by the downstream part of the wheel arch in a horizontal plane towards the side of the model. The boundary layer separates on the downstream inner edge of the running surface of the wheel. This separation bubble reaches the underbody flow that stretches it towards the underbody and the wake, giving rise to vortex E (see Fig. 6). Based on computations including the wheel axis in the geometrical model (for model in Fig. 3b) vortex E was found to be independent on the mechanical elements in the wheelhouse.

Path lines started below Section 3 of the wheelhouse leading edge "a", i.e. in front of the lower part of the wheel exposed to the wind are deflected upwards by the wheel (see Fig. 8b). The same pattern of inflow was observed and published by several researchers (Eloffson et al., 2002; Fabijanic, 1996; Cogotti, 1983; Oswald and Browne, 1981; Hucho, 1998; Wiedemann, 1996) but no explanation or model was given about the flow structure. The interaction of up-flow and the running surface of the wheel moving in the opposite direction to the flow cause boundary-layer separation over the upper part of the running surface of the wheel. The separation bubble elongates towards the inner part of the wheelhouse and reaches the inner wall (base point of vortex A, see Fig. 7). In the outer part of the separation bubble (vortex A), air flows towards the middle of the vehicle model. After reaching the inner wall air seems to flow in the middle of the vortex in the opposite direction towards the side of the model. When vortex A reaches the flow beside the side of the model, it will be deflected in the direction of the outside flow and elongated. Vortex A, in which the sense of rotation is opposite to that of the wheel, is shown in Figs. 6 and 8. Its characteristics are sensitive mainly to the non-uniform pressure field between the lower and side openings of the wheelhouse.

Inside the wheelhouse behind the leading edge "a" (see Fig. 6) boundary layer separation causes vortex H, the sense of rotation of which corresponds to that of the wheel. In the case of larger yaw angle of the wheel approaching flow, vortex H will be complemented by the vortex caused by boundary layer separation along the lower horizontal edge of the inner wall (edge "b" in Fig. 6). For the same reason vortex C develops over the upstream edge of wheel arch "d" in Fig. 6, particularly in the case of a rounded lower longitudinal edge of the vehicle body as a continuation of vortex H. At a higher point in the wheel arch edge "d" vortex C separates and as a consequence of the interaction with the outside flow it is turned beside the upper part of the wheel in the direction of flow. It is an interesting characteristic of vortex C that it causes no significant inflow into the wheelhouse, which is demonstrated also by Fig. 7.

3.4. Flow field inside of wheelhouse

In the interior of wheelhouse the flow is characterized mainly by vortices A, B, H, and E. The size of vortex A depends on the quantity of air entering the wheelhouse below Section 3 of the leading edge and turned upwards by the rotating wheel. If the yaw angle of the wheel-approaching flow is small, i.e. the fore-body length is large (see Section 3.2) as is the flow rate entering vortex A, so this vortex dominates the flow field in the wheelhouse. In this case vortex B does not emerge, the air entering the wheel arch under Section 1 of edge "a" will follow the same path as the flow entering under Section 2, strengthening vortex E. With increasing yaw angle the flow rate of air entering the wheel arch under Section 3 of edge "a" decreases, so the upstream part of the wheelhouse is filled by the air entering the wheelhouse under Section 1 and forming vortex B.

3.5. Downstream part of the flow field, outflow from the wheelhouse

A large part of the air entering the wheelhouse flows out through vortex A: in the outer part of it air flows inside the wheelhouse and in the internal part of the vortex air flows

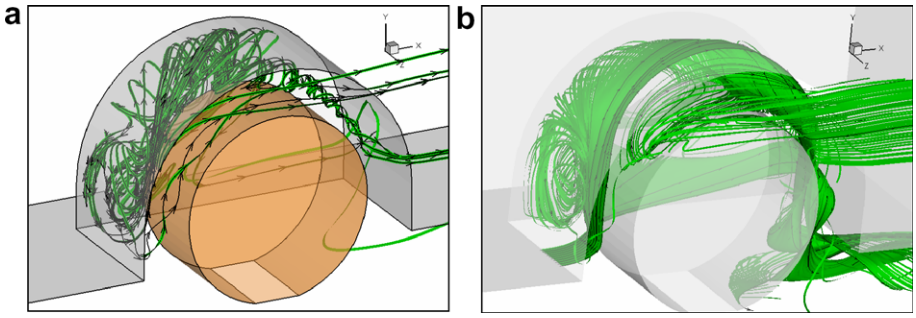

Fig. 8. Streamlines in wheelhouse for (a) stationary wheel and (b) rotating wheel. Flow from left to right.

out (see Fig. 8b). If vortex B exists (for shorter fore-body, larger yaw angle), considerable outflow also occurs in this vortex. Air leaving the wheelhouse through vortex E gets in the underbody flow and – if the rear wheel is considered – it might influence the flow field of the wake (Fig. 7).

It should be noted that vortex tubes A, B, C, E elongate when entering the high-velocity flow beside the side wall and in the underbody gap; consequently they will be dissipated and disappear quickly. This process is demonstrated by the streamlines of the calculated flow field. In fact, vortices A and C can be seen at the front wheelhouses of vehicles in rainy weather when water drops dispersed by the wheels visualize the flow field.

In the downstream part of the wheel arch outflow occurs in the gap between the wheel and the wheel arch. As a consequence of boundary layer separation over the downstream edge of the wheel arch vortex S develops (see Fig. 9 where Q and total pressure iso-surfaces indicate the presence of this vortex). If vortex B is present, it can influence the size of vortex S.

3.6. The influence of the shape as well as the rotation of the wheel on flow structures

The profiles of the wheels are in general rounded up, but for several wheel models the running surface protrudes resulting in a reduction of water dispersion in rainy weather. The sides of the running surface form edges around the wheel, promoting boundary-layer separation. Even in the case of rounded-up profiles, the radius of curvature is so small that boundary layer separation occurs. That is why no significant changes in flow field were observed when the effect of rounding-up of the profile of a wheel rotating in a wheelhouse was investigated.

If the width of the gap between the running surface of the wheel and the wheel arch significantly exceeds the boundary layer thickness over the wheel perimeter, then for small yaw angle of wheel approaching flow the rotation of the wheel does not radically change the flow structures in the wheelhouse with respect to the stationary wheel. The characteristics of the boundary layer over the running surface of the wheel (which depends on the rotation of the wheel) mainly influence the position of vortex A: for a stationary wheel the vortex is shifted downstream, i.e. the rotation of the wheel shifts the boundary layer separation upstream (see Fig. 8).

In the case of a stationary wheel, the rotating mass of air in vortex A leaves the wheelhouse above the downstream part of the wheel (leading to an increase in lift), while in the case of a rotating wheel it is shifted in the upstream direction, decreasing slightly drag (see Fig. 8).

3.7. Dynamically significant flow structures

In the previous sections the flow field was described by analysis of its topography using the vortex skeleton method. In this chapter the flow field will be analyzed from the point of view of aerodynamic forces that are influenced mainly by vortices, because these can cause pressure change or fluctuation over parts of neighboring solid surfaces. That is why differentiation of dynamically significant structures and "dead areas" of the flow field is useful (Farge et al., 2003). The latter zones are in general separation bubbles in which the velocity is about 20%, i.e. the dynamic pressure is 4% of that of flow beside the body. Separation bubbles are separated from the outside flow by a shear layer, so the total pressure (head) is rather small in it.

Dynamically significant flow structures were detected by investigating the spatial distribution of two quantities, one being the total pressure (head) of the flow, the other being the second invariant of the velocity gradient tensor (Q) (Jeong and Hussain, 1995; Hussain, 1983; Hussain, 1986).

Fig. 9 shows the $Q \cdot (D/U_{\text{free}})^2 = 20$ iso-surfaces in the wheelhouse of the model with 1D fore-body length. It can be seen that vortices H, C, L, R and E are regarded as dynamic structures. According to the experience of the authors, the existence of these structures and their position in the wheelhouse is practically independent of the geometry of the vehicle models (see Fig. 10).

It can be observed that Q iso-surfaces appear only in the high-velocity areas of the flow field; in separation bubbles

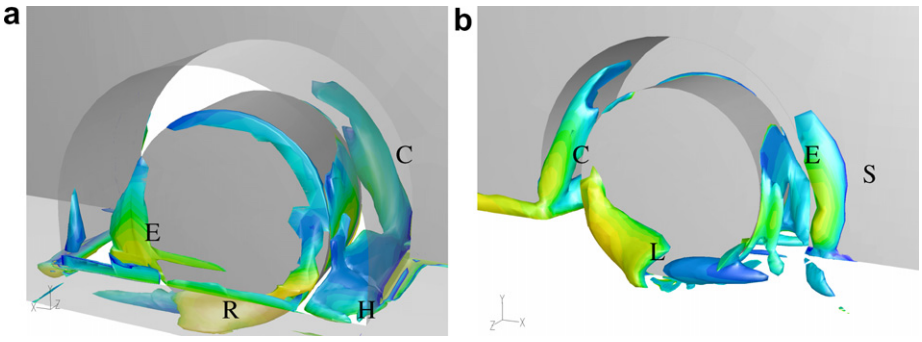

Fig. 9. $Q \cdot (D/U_{\text{free}})^2 = 20$ iso-surfaces in the wheelhouse of a model with 1D fore-body length: (a) inner view, flow from right to left; (b) outer view, flow from left to right.

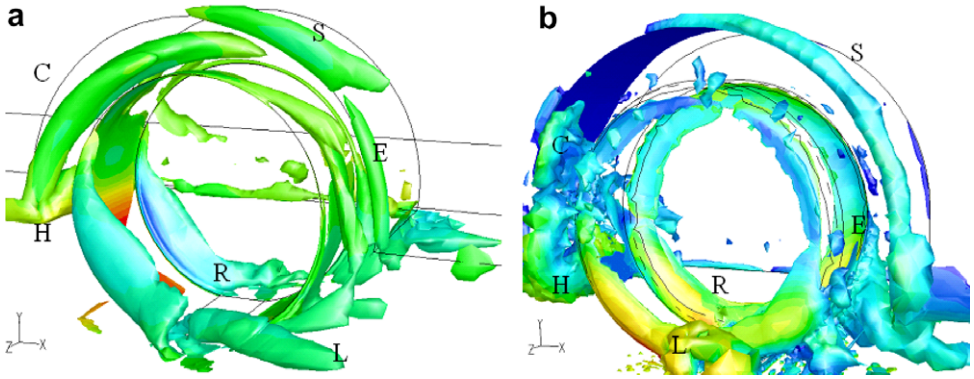

Fig. 10. Iso-surfaces of $Q \cdot (D/U_{\text{free}})^2 = 20$ in wheelhouses of (a) infinite fore-body length body, (b) 2D fore-body length body.

where the velocities are smaller they do not indicate flow structures like vortices A and B.

This is why the traditional representation method was also used. Because of the vorticity (curl) towards the "axes" of vortices, the total pressure decreases, so the off-solid-surface low total-pressure iso-surfaces probably enclose vortices. Fig. 11 shows for the same flow field as Fig. 9 iso-surfaces belonging to low total pressure values. Vortices L and R close to the ground on both sides of the wheel as well as vortex H can be seen clearly: vortices A and B – which were not detected by any iso-values of the Q iso-surfaces (see Fig. 9) – are also indicated by this method. A large area indicates vortex E developing behind the wheel and turning downwards into the underbody gap. Differences were experienced between the two methods for tracing flow structures. The reason for this is that a high value of Q indicates large values of local vorticity (curl) while (besides vorticity) total pressure is also related to losses; thus it detects dead areas, as well. However, here it also shows its deficiencies at representing rotating masses of fluid. So, the same low total pressure can indicate strong vortices (dynamically active flow structures) in high-velocity flow (e.g. vortices L and R) or weak vortices (e.g. A and B) without considerable impact on the aerodynamic forces, inside a separation bubble separated from the outside flow by a shear layer, causing low total pressure (head).

Dynamically significant structures that influence the flow field considerably can be expected in parts of the flow field where velocities are relatively high, therefore these structures can be detected by Q iso-surfaces.

3.8. The effect of wheelhouse geometry on the flow field

The position and intensity of the individual flow structures shown in Fig. 6 depend mainly on the wheelhouse geometry. As it was shown previously, the intensity and position of vortices A and B depend predominantly on the yaw angle of the wheel approaching flow, which is a function of the fore-body length, while the position and size of vortices H, C, R, L and E show only minor changes. In this section the influence of wheelhouse geometry (diameter and width of the wheel arch with respect to wheel diameter and width) on the structure of the flow field will be discussed. When reducing the diameter of the wheel arch the width of the gap between running surface and wheel arch decreases, so the flow rate of air entering this gap and producing vortex A decreases, while vortex B, fed by unchanged inflow in the internal part of the wheelhouse, comes more and more to dominate. As a consequence of the reduction of the wheelhouse diameter the wheel gradually closes the openings towards the side of the body so the flow field in the wheelhouse resembles more and more that

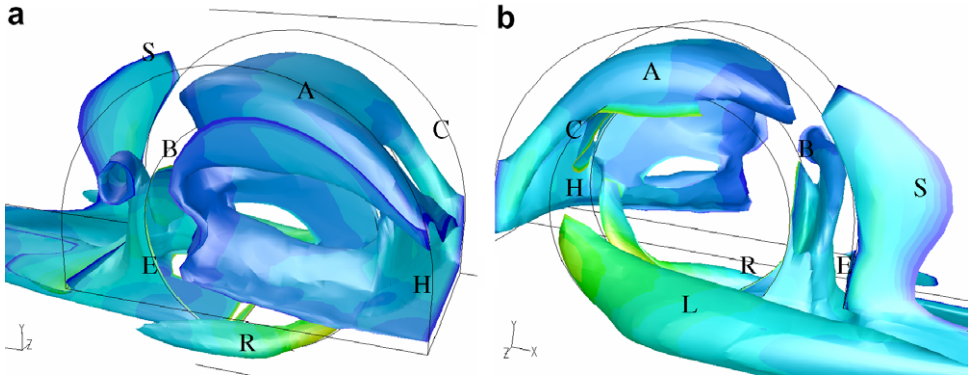

Fig. 11. Iso-surfaces of total pressure in the wheelhouse of a vehicle model with 1D fore-body length: (a) view from inside, (b) view from outside.

of a cavity opened from below, in which vortex A disappears and vortex B dominates (Komerath et al., 1987), i.e. the impact of wheel rotation on the flow disappears. Vortex E behind the wheel and vortices H and C remain but their size decreases with the size of the gap between the wheel and wheel arch.

A decrease in the width of the wheel arch (depth of the wheelhouse) effects mainly vortex B through a reduction of the flow rate entering the wheelhouse under Sections 1 and 2 of the leading edge "a" (see Fig. 6). If the diameter of the wheel arch is kept constant while the depth of the wheelhouse decreases, the flow in the wheelhouse becomes more and more similar to that of a cavity opened towards the side of the body: vortex C becomes more and more the dominant flow structure and B disappears. The inflow of air in front of the wheel remains unchanged so vortex A keeps its dominant position in the upper part of the wheelhouse. This upward flow influences the flow in vortex C. The part of vortex E which is inside the wheelhouse is fed by air entering the wheelhouse between the wheel and the inner wall, its size and intensity decreases with decreasing wheelhouse depth. However, the part of vortex E which is positioned in the underbody gap elongated towards the wake of the vehicle model is further fed by the air entering from the sides of the vehicle model via a boundary layer separation from its lower longitudinal edge towards the underbody gap.

4. Analysis of aerodynamic forces

4.1. Distribution of forces over the body: effect of wheel and wheelhouse

In this section the surface of the basic body and simplified car body will be divided into parts (see Fig. 7) and, on the basis of flow fields calculated with the validated CFD model, aerodynamic forces acting on these parts were determined by integrating the pressure and shear stress distribution over them. So the contribution of different body elements, wheel and wheelhouse to the overall aerodynamic force coefficients was determined. The results reported here are for $Re = 8.5 \times 10^5$ calculated with wheel diameter and undisturbed flow velocity. Table 2 shows the drag and lift coefficients for different parts of the basic model having no wheels and wheelhouses. Table 3 includes the same values for a simplified car model having wheels and wheelhouses. The ground was moving in both cases. Fig. 7 shows the individual parts on the model for which the force coefficients were determined separately (see Table 4).

Table 2
Aerodynamic force coefficients related to parts of the body of basic model

	Drag coefficient	Lift coefficient
Front face	0.107	0.198
Base	0.148	0
Roof	0.011	0.375
Underbody	0.008	−0.539
Total	0.274	0.034

Table 3
Aerodynamic force coefficients related to parts of the body of simplified car model

	Drag coefficient	Lift coefficient
Front face	0.147	0.211
Base	0.157	0
Roof	0.010	0.402
Underbody	0.007	−0.432
Subtotal	0.321	0.182
Wheelhouse	0.025	−0.091
Wheel	0.097	0.100
Total	0.443	0.191

Table 4
Aerodynamic force coefficients related to parts of the body of a simplified car model with closed wheelhouses

	Drag coefficients	Lift coefficients
Fore-body	0.180	0.093
Base	0.146	0
Roof	0.01	0.5
Underbody	0.006	−0.366
Wheel	0.065	0.010

In both tables the front face includes the vertical wall and the rounded-up leading edges around the front face. Thus, the vertical force acting on the front face is the resultant of the lift and downward force acting on the upper and lower horizontal leading edges, respectively. When analyzing the figures in the tables it can be concluded that the wheels and wheelhouses increase pressure on the front face, causing a 37% increase in fore-body drag and decrease the pressure over the base that results in 6% increase in base drag. This change can be explained by the effect of the lower part of the wheels that reduce the velocity of underbody flow and increase in this way the pressure on the lower side of the fore-body. The minor change of the base drag indicates the interaction of the wake of the wheels (mainly vortex E) and that of the body. The overall increase of drag acting on the simplified car model as a consequence of the wheels and wheelhouses is 62% with respect to that of the basic model. Of this, 17.2% is the increase of drag acting on the body (predominantly the increase of the sum of fore-body and base drag). In addition to this, the drag acting on the wheels and wheelhouses causes individually 35.6% and 9.1%, respectively or 44.7% increase in overall drag. It can be concluded that one-quarter and three-quarters of the significant increase in drag can be assigned to an increase of drag on the body and on the wheel and wheelhouse, respectively. The majority, 57.4%, of increase is due to the drag acting on the wheel.

When analyzing the lift forces it can be stated that the wheels and wheelhouses cause a significant increase of lift force (the lift coefficient increased from 0.034 to 0.191 in case of the present model). Significant lift force acts on

the wheels, which is nearly equal to their drag. Since the downward force acting on the wheelhouse filled with a separation bubble practically compensates the lift acting on the upper surface of the wheel, the overall increase of the lift is mainly due to the lift acting on the lower part of the wheel exposed to the underbody flow and due to the reduction of underbody flow velocity by the wheels that causes a significant change of lift forces both on the front face and on the roof as well as a decrease of downward force acting over the underbody. It can be concluded, that, in the case of drag, the majority of the increase is caused by the force acting on the wheels and wheelhouses, the increase of lift forces is a consequence of change of lift force acting on the body, and the lift generated on the lower part of the wheel.

4.2. Effect of closing of openings of wheelhouse

Investigations were carried out to discover the effect of closing the wheelhouse openings towards the side and downwards on the aerodynamic drag and lift. Numerical simulations were carried out using the simplified car model shown in Fig. 3c. The wheels rotated in all configurations. The configurations investigated were:

- closed bottom openings, open side gap;
- closed side gap, open bottom opening;
- closed side gap and bottom opening (no wheelhouse);
- open wheelhouse without wheel;
- basic model without wheel and wheelhouse;
- simplified model with wheel and wheelhouse.

The results of investigations are summarized in Fig. 12 where the change of drag and lift forces is shown with respect to the corresponding values for the simplified (reference) model with wheels and wheelhouses. The removal of wheels and wheelhouses results in a significant reduction of both drag and lift. When removing only the wheels (open wheelhouses) the reduction of drag is much smaller but the largest lift reduction was found for this configuration. It is caused by low pressure in the separation bubbles in the wheelhouses not compensated for by a lift force acting on the wheels.

When closing the wheelhouse (keeping the rotating wheel) the drag is smaller by 12% than that of the reference case, showing the limit of the drag reduction potential of reducing the wheelhouse sizes for the present vehicle model. The lift force is about the same as for the reference configuration. Since we have found (see above) that for the reference case the lift force is caused by the pressure distribution over the body (the vertical forces acting on wheel and wheelhouse compensate each other), it can be concluded that practically only the lower part of the wheels that are exposed to the underbody flow and not the upper part of the wheel and the wheelhouse cause the change of the flow field.

The closing of the bottom openings of the wheelhouses results in modest decrease of drag and considerable increase in lift with respect to reference configuration. The flow field in the wheelhouse (shown in Fig. 13a) is completely different from that observed in open and only from the side closed wheelhouses. This experience shows the significance of the bottom openings of the wheelhouse in developing the flow field within it. Air enters the wheelhouse in the downstream gap between the wheel and wheel arch and leaves it sideways through the upstream gap. In addition, the pressure below the ambient over the covering of the bottom opening increases the lift.

Closing the side gap for the open bottom opening caused the smallest drag reduction and the largest increase in lift. The structure of the flow field can be seen in Fig. 13b. Vortices L, R, H, A and E can be found, C and B disappeared. The vanishing of vortex C is trivial, that of vortex B can be explained by the increase and dominance of vortex A. The significant increase of lift can be explained by the increase of pressure in the wheelhouse as a consequence of the closing of outflow from the wheelhouse through vortices A and B.

The results of the investigations indicated that for body configurations that include wheels, covering of the wheelhouse openings results in drag reduction and increase of lift. The effect of closing the side gaps causes only minor change in flow structure while closing the bottom opening causes fundamental changes. This seems to support the view that flow in the wheelhouse interacts mainly with the underbody flow, and that the effect of flow adjacent to the side wall is of secondary importance.

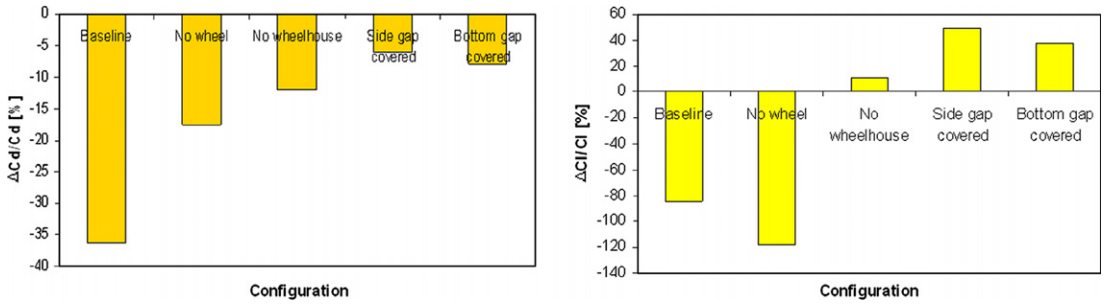

Fig. 12. Effect of closing the wheelhouse openings on drag and lift forces in comparison with the model with wheel and open wheelhouse.

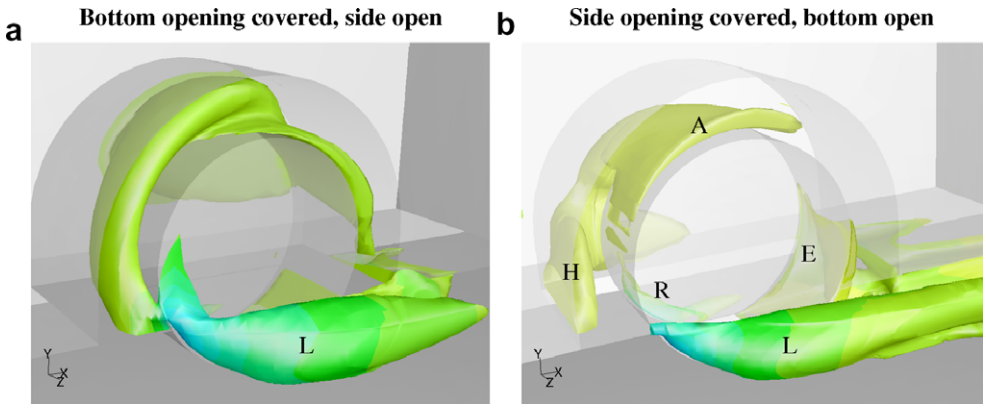

Fig. 13. Structure of flow field represented for the case of covering wheelhouse openings; (a) and (b) show iso-surfaces of total pressure; Flow from left to right.

5. Conclusions

This work reports the results of numerical modeling of the flow fields past wheels in wheelhouses of passenger cars by means of RANS approach. The validation of the numerical models was carried out by comparing the results of simulations (pressure distributions, aerodynamic forces) to those of experiments published in the literature. Investigations were made to determine the existence of large scale unsteadiness by URANS computations. These resulted in a quasi steady flow field that enabled the application of RANS approach for further investigation.

Based on the simultaneous application of three alternative vortex detection methods and the surface pattern "wall-streamline" analysis, a procedure was applied using the concept of vortex skeleton method and applied to detect dynamically significant structures, vortices in the flow field in wheelhouses. The complex analyses of the flow field resulted in the definition of several vortices in the wheelhouse, out of which the existence of six vortices were found to be independent of the change of geometry of the vehicle body apart from the wheelhouse.

From the viewpoint of flow in wheelhouses, i.e. the extent and strength of characteristic vortices, the main effect of the car body is the deflection of underbody flow towards the sides of the car, resulting in a yaw angle of attack when approaching the wheel. The wheelhouse flow has very little correlation with the flow along the sides of the vehicle.

With the present modeling approach it was found that the rotation of the wheel has a relatively small effect on the structure of the flow field if the gap between the wheel and the wheelhouse cavity is larger than the thickness of the boundary layers.

Aerodynamic forces acting on various parts of the simplified vehicle body were determined on the basis of the results of RANS modeling. In this way the change in the drag and lift force due to wheel and wheelhouse could be analyzed. It was found that the substantial increase of drag force is due mainly to the drag acting on the wheel and to the change of fore-body and base drag caused mainly by the wheel influencing the underbody flow. The increase of lift force, on the other hand, is due to the lift acting on the wheel and the modification of flow field around the body by the wheel and is negligibly affected by the flow conditions inside the wheelhouse.

The structure of the flow field resulting from changing the diameter and width of the wheelhouse cavity was examined, and the changes reported and explained. Another investigation was made on the coverage of the side and lower openings of the wheelhouse cavity. It was found that the flow structure and the aerodynamic forces changed most when the lower opening was covered and changed only slightly when the side opening was closed. This led to the conclusion that the flow field, and thus the aerodynamic forces in wheelhouse are mainly influenced by the underbody flow through the lower opening of the wheelhouse and is slightly sensitive to the side gap coverage.

Based on the results of numerical investigations, general conclusions can be drawn and measures developed to determine the characteristics and control of the aerodynamics of wheelhouses.

References

Axon, L., Garry, K., Howell, J., 1998. An Evaluation of CFD for Modelling the Flow Around Stationary and Rotating Isolated Wheels. Society for Automotive Engineers, Paper 980032, Detroit, pp. 205–215.

Axon, L., Garry, K., Howell, J., 1999. The Influence of Ground Condition on the Flow Around a Wheel Located Within a Wheelhouse Cavity. Society of Automotive Engineers, Inc. 1999-01-0806, pp. 149–158.

Basara, B., Beader, D., Przulj, V. Numerical simulation of the air flow around a rotating wheel, in: 3rd MIRA International Vehicle Aerodynamics Conference, 18/19 October 2000, Rugby, UK.

Cogotti, A., 1983. Aerodynamic characteristics of car wheel. Impact of aerodynamics on vehicle design. Int. J. Vehicle Des. SP3, 173–196.

Eloffson, P., Bannister, M., 2002. Drag reduction mechanisms due to moving ground and wheel rotation in passenger cars. Society for Automotive Engineers, paper, 2002-01-0531, pp. 185–198.

Fabijanic, J., 1996. An experimental investigation on wheel-well flows. Society for Automotive Engineers, paper, 1996, 960901, pp. 161–172.

Fackrell, J.E., Harvey, J.K., 1973. The flow field and pressure distribution of an isolated road wheel. Adv. Road Vehicle Aerodyn., 155–164.

Farge, M., Schneider, K., Pellegrino, G., Wray, A.A., Rogallo, R.S., 2003. Coherent vortex extraction in three-dimensional homogeneous turbulence: Comparison between CVS-wavelet and POD-Fourier decompositions. Phys. Fluids 15 (10), 2886–2896.

Hanjalić, K., 2005. Synergy of experiments and computer simulations in research of turbulent convection. Int. J. Heat Fluid Flow 26, 828–842.

Hedges, L.S., Travin, A.K., Spalart, P.R., 2002. Detached-eddy simulations over a simplified landing gear. J. Fluids Eng. 124, 413–423.

Hucho, W.H., 1998. Aerodynamics of Road Vehicles. Butterworth and Co. Publishing, Boston.

Hussain, A.K.M.F., 1983. Coherent structures-reality and myth. Phys. Fluids 26, 10.

Hussain, A.K.M.F., 1986. Coherent structures and turbulence. J. Fluid Mech. 173, 303–356.

Jeong, J., Hussain, F., 1995. On the identification of a vortex. J. Fluid Mech. 285, 69–94.

Komerath, N.M., Ahuja, K.K., Chambers, F.W., 1987. Prediction and measurement of flows over cavities – a survey. In: Proceedings of the AIAA 25th Aerospace Sciences Meeting, Reno, Nevada, January.

Lajos, T., Preszler, L., Finta, L., 1984. A wind-tunnel investigation of mud deposits on the body of a bus. Int. J. Vehicle Des. 5 (6), 693–703.

Lajos, T., Preszler, L., Finta, L., 1988. Styling and Aerodynamics of Buses. Int. J. Vehicle Des. 9 (1), 1–15.

Leschziner, M.A., 2006. Modelling turbulent separated flow in the context of aerodynamic applications. Fluid Dyn. Res. 38, 174–210.

Liu, Y., Tucker, P.G., Iacono, G.L., 2006. Comparison of zonal RANS and LES for a non-isothermal ribbed channel flow. Int. J. Heat Fluid Flow 27, 391–401.

McManus, J., Zhang, X., 2006. A computational study of the flow around an isolated wheel in contact with the ground. Trans. ASME 128 (May), 520–530.

Mears, A.P., Dominy, R.G., Sims-Williams, D.B., 2002. The air flow about an exposed racing wheel. Society for Automotive Engineers, paper, 2002-01-3290, pp. 37–43.

Menter, F.R., 1994. Two-equation eddy-viscosity turbulence models for engineering applications. AIAA J. 32 (8), 1598–1605.

Merker, E., Berneburg, H., 1992. Über die Simulation der Straßenfahrt eines PKW in einem Windkanal durch bewegten Boden und drehende Räder. Tagung Aerodynamik des Kraftfahrzeugs, Essen.

Morelli, A., 1969. Aerodynamic actions on an automobile wheel. In: Proceedings of the Symposium on Road Vehicle Aerodynamics. City University, London.

Oswald, L.J., Browne, A.L., 1981. The airflow field around an operating tire and its effect on tire power loss. SAE Paper 810166, pp. 117–132.

Perry, A.E., Hornung, H., 1984. Some Aspects of Three-Dimensional Separation, Part II: Vortex Skeletons. Zeitschrift für Flugwissenschaften und Weltraumforschung, 8, Heft 3.

Perry, A.E., Chong, M.E., Cantwell, B.J., 1990. A general classification of three-dimensional flow fields. Phys. Fluids A 2 (5), 765–777.

Régert, T., Lajos, T., 2003. Investigation of flow field past rotating wheels of cars. In: Proceedings of Conference on Modelling Fluid Flow (CMFF), pp. 387–394.

Régert, T., 2003. Visualization studies in TU Dresden NWK. Technical report.

Rodi, W., 1997. Comparison of LES and RANS calculations of the flow around bluff bodies. J. Wind Eng. Ind. Aerodyn., 55–75.

Schmidt, S., Thiele, F., 2002. Comparison of numerical methods applied to the flow over wall-mounted cubes. Int. J. Heat Fluid Flow 23, 330–339.

Shih, T.-H., Liou, W.W., Shabbir, A., Yang, Z., Zhu, J., 1995. A new k–ε eddy-viscosity model for high reynolds number turbulent flows – model development and validation. Comput. Fluids 24 (3), 227–238.

Skea, A.F., Bullen, P.R., Qiao, J., 1998. The use of CFD to predict air flow around a rotating wheel. In: 31st International Symposium on Automotive Technology and Automation, Düsseldorf, pp. 187–196.

Skea, A.F., Bullen, P.R., Qiao, J., 2000. CFD simulations and experimental measurements of the flow over a rotating wheel in a wheel arch. Society for Automotive Engineers, paper, 2000-01-0487, pp. 115–123.

Wickern, G., Zwicker, K., 1995. Zum Einfluß von Rädern und Reifen auf den aerodynamischen Widerstand von Fahrzeugen. Tagung ''Aerodynamik des Kraftfahrzeugs'', Haus der Technik e. V., Essen.

Wiedemann, J., 1996. The influence of ground simulation and wheel rotation on aerodynamic drag optimization – Potential for reducing fuel consumption. Society for Automotive Engineers, paper 960672.

Wolfshtein, M., 1969. The velocity and temperature distribution of one-dimensional flow with turbulence augmentation and pressure gradient. Int. J. Heat Mass Transfer 12, 301–318.